HHS Public Access

Author manuscript

Biomed Phys Eng Express. Author manuscript; available in PMC 2018 October 01.

Published in final edited form as:

Biomed Phys Eng Express. 2017 October ; 3(5): 055001–. doi:10.1088/2057-1976/aa87c2.

A Phantom Study of Terahertz Spectroscopy and Imaging of Micro- and Nano-diamonds and Nano-onions as Contrast Agents for Breast Cancer

Tyler Bowman[a,*], **Alec Walter**[a], **Olga Shenderova**[b], **Nicholas Nunn**[b], **Gary McGuire**[b], and **Magda El-Shenawee**[a]

[a]University of Arkansas, Department of Electrical Engineering, 3217 Bell Engineering Center, Fayetteville, AR, USA 72701

[b]Adámas Nanotechnologies, Inc., 8100 Brownleigh Dr Suite 120, Raleigh, NC 27617

Abstract

THz imaging is effective in distinguishing between cancerous, healthy, and fatty tissues in breast tumors, but a challenge remains in the contrast between cancerous and fibroglandular (healthy) tissues. This work investigates carbon-based nanoparticles as potential contrast agents for terahertz imaging of breast cancer. Microdiamonds, nanodiamonds, and nanometer-scale onion-like carbon are characterized with terahertz transmission spectroscopy in low-absorption backgrounds of polydimethylsiloxane or polyethylene. The refractive index and absorption coefficients are calculated based on the measured electric fields. Nanodiamonds show little effect on the terahertz signal, microdiamonds express resonance-like, size-dependent absorption peaks, and onion-like carbon provides a uniform increase in the optical properties even at low concentration. Due to its strong interaction with terahertz frequencies and ability to be activated for selective binding to cancer cells, onion-like carbon is implemented into engineered three-dimensional breast tumor models composed of phantom tissue mimicking infiltrating ductal carcinoma surrounded by a phantom mimicking healthy fibroglandular tissue. This model is imaged using the terahertz reflection mode to examine the effectiveness of contrast agents for differentiation between the two tissue types. In both spectroscopy and imaging, a 10% concentration of onion-like carbon shows the strongest impact on the terahertz signal and holds promise as a terahertz contrast agent.

Keywords

terahertz; medical imaging; onion-like carbon; nanodiamonds; spectroscopy; breast cancer

1 Introduction

Electromagnetic detection of breast cancer encompasses a wide field of frequency ranges and techniques [1]. In addition to well-known screening and treatments in X-ray technology, magnetic resonance imaging, and radiation therapy, investigations into the properties of breast tissues have spanned a broad range of frequencies in the electromagnetic spectrum.

*Tyler Bowman, tcbowman@uark.edu.

Early investigations found clear distinctions in the dielectric permittivity and conductivity between tumors, tumor-adjacent tissue, and healthy breast tissue from 20 kHz (very low frequency, VLF) to 100 MHz (very high frequency, VHF) [2], between malignant and healthy tissue from 50 MHz (VHF) to 900 MHz (microwave) [3], and between breast cancer metastasis in lymph nodes compared to normal lymph nodes from 0.5 GHz to 30 GHz [4]. However, a study at 3.2 GHz showed significant overlap in permittivity and conductivity between fibrous, benign, and malignant tumors [5], and two large-scale studies from 0.5 to 30 GHz showed wide permittivity variations in healthy fibrous tissue depending on the fat concentration [6], and that the permittivity of malignant breast cancer and densely fibrous tissue (little to no fat) differs by less than 10% [7]. This lack of contrast represents a key challenge in microwave detection of cancer.

At the visible and infrared frequencies, investigation of the properties of breast cancer showed similar challenges as in the microwave range [8, 9]. As a result, most modern implementations of optical frequencies for breast cancer detection depend on fluorescence using fluorophores and contrast agents or on auto-fluorescence of specific cellular structures [10-12]. These fluorescence imaging applications are mostly focused on intraoperative (i.e. in an operation room) differentiation between malignant and healthy tissue, which is a primary medical concern in breast cancer surgeries. Intraoperative differentiation between cancer and heathy tissues as a complementary process to pathology was also investigated using x-ray imaging of surgically removed tumors (specimen radiography). Radiography for tumor margin assessment was shown to be effective [13], but several studies have reported that it can miss remnant cancer when compared to pathology [14], suffers from size and accuracy in smaller tumors [15], and has low sensitivity [16]. Thus, there is still a need to develop techniques for accurate intraoperative assessment of breast tumor boundaries following a surgical procedure.

The terahertz (THz) frequency band is currently being investigated as an alternative method for intraoperative assessment of breast cancer. THz frequencies were reported to be nonionizing and safe for biological applications [17] with higher image resolution compared to the microwave band. A comparison between optics and THz imaging for freshly excised tissues, favoring THz imaging, was reported in [18]. Furthermore, THz imaging was successfully applied to a wide range of cancer applications of freshly excised tissues of the breast [19-20], skin [21], and brain [22], and for fixed tissues of the breast [23-25] and liver [26]. Reported THz spectroscopy of freshly excised breast cancer tissue from 0.15 to 2 THz showed distinction between the refractive index of cancer, fibroglandular, and fat tissues [19]. Likewise, THz pulsed imaging of human breast cancer has shown clear distinctions between these tissue types in both fresh and formalin-fixed, paraffin-embedded (FFPE) tumors [20],[23-25]. While THz for detecting cancer margins has shown a potential, it is not meant for use in patient diagnosis, screening, or replacing the pathology assessment of surgical tissues. If successful, THz imaging has a potential to provide a rapid intraoperative assessment of excised tumors.

However, the reported THz works of freshly excised tissues [19] showed a relatively little difference in the absorption of cancer and fibroglandular tissues. The idea here is to implement contrast agents to improve the distinction between cancerous and healthy tissues

in THz imaging. For example, gold nano-rods (GNRs) were shown to provide an approximate 20% increase in the THz response of A431 epidermoid carcinoma cells in a petri dish when activated with an infrared laser [27]. Likewise, superparamagnetic iron oxide nanoparticles (SPIOs) were utilized in conjunction with localized magnetic fields and MRI to increase THz contrast by an unreported amount in pulsed time-domain imaging of mouse ovarian cancer [28] and by 35% for 0.2 THz continuous wave imaging of water [29]. However, both GNRs and SPIOs require the use of an external non-THz source to generate the contrast improvement in the particles. Gadolinium oxide has also shown potential for contrast enhancement in THz spectroscopy [30], and indium nitride was investigated in modeling of skin cancer [31], but neither particle was tested in THz imaging.

This work investigates the use of carbon-based particles with dimensions on the micrometer and nanometer scale as potential THz contrast agents for imaging breast tumors. Fluorescent high pressure high temperature (HPHT) nanometer-scale diamonds (nanodiamonds, NDs) containing color centers and onion-like carbon (OLC, also called carbon nano-onions) conjugated with a fluorophore were previously utilized for fluorescence in optical frequencies [32,33]. NDs were shown to be biologically safe for extended times using injections of 100 nm functionalized particles over a period of 5 months in mice [34]. Additionally, small NDs in the 5 nm range induced relatively little genetic toxicity compared to other nanoparticles [35], and in general NDs have shown insignificant toxicity in all studies [36]. Meanwhile, OLC was shown to have distinctly high absorption at frequencies from 20 Hz to 3 THz, excluding the frequency ranges from 3 GHz to 8 GHz and 53 GHz to 100 GHz [37,38]. OLC was also shown to be an effective absorber in low quantities at infrared frequencies from 10 to 230 THz [39]. OLC can be functionalized to selectively bind the surface of cancer cells [40,41] and was shown to induce less inflammatory response and cell toxicity than carbon nanotubes with similar functionalization [41,42]. OLC of size 30 nm in concentrations of 0.6 mg/L and 6 mg/L was reported to have far less genetic toxicity in human fibroblasts than carbon-nanotubes in one tenth of the concentration [42]. Similar results were seen for 5 nm OLC in concentrations of 30, 300, and 3000 μg/mL in rat fibroblasts with minimal loss of cell viability (15% at the highest concentration) [43], and additional studies of OLC at lower concentrations showed insignificant toxicity when tested with different kinds of functionalization [44]. In addition to having low toxicity, these carbon-based particles cost less than organic dyes or quantum dots used for nanoparticle functionalization by an order of magnitude [36]. However, these particles have yet to be investigated for effectiveness in tissue at THz frequencies.

In this work, microdiamonds, nanodiamonds, and OLC are investigated as potential image contrast factors by first using THz spectroscopy to examine the optical properties of each particle type with multiple sizes, preparations, and concentrations while distributed in polydimethylsiloxane (PDMS) or polyethylene. These polymers have relatively low absorption compared to fresh tissues and allow for characterization of the particles without significant signal loss in the surrounding medium. The particles providing the greatest impact on the THz signal are then examined in breast cancer phantom tissues. Phantom tissues are used here for their highly-controlled nature, ease in implementing the particles in different concentrations, and low cost.

Phantoms were utilized for some time in microwave frequency modeling of breast cancer and other tissue types [45,46]. However, the use of phantoms for THz applications in the literature so far was limited to solid phantoms with limited ability to mimic tissue properties [47] or highly tunable non-solid oil-water emulsions [48]. This work makes use of highly tunable solid phantoms for breast cancer tissues recently developed by the authors as reported in [49] and [50]. To the best of our knowledge, the current paper is the first work to demonstrate OLC and other carbon-based particles immersed in breast phantom tumors as potential THz image contrast agents.

This work is organized as follows: methodology and materials in Section 2; results of particle characterization in Section 3; results of breast phantom tumor imaging with and without OLC particles in Section 4; and discussion and concluding remarks in Section 5.

2. Methodology and Materials

2.1 Terahertz Spectroscopy and Imaging Setup

This work was conducted using the TPS Spectra 3000 pulsed THz imaging and spectroscopy system (purchased from TeraView Ltd., UK) at the University of Arkansas. The diagram of the system can be seen in Fig. 1. An 800 nm pulse from a Ti:Sapphire laser is used to excite a biased THz emitter consisting of a photoconductive antenna on a GaAs substrate. The resulting THz signal is either transmitted through a sample placed in the system as seen in Fig. 1a or directed using mirrors to reflect off the sample as seen in Fig. 1b and is then collected at a THz receiver with the same structure as the emitter. The unobstructed THz pulse is given in Fig. 1c, while the Fourier transform of the pulse is given in Fig. 1d. The width of the time-domain pulse is ~280 fs at $1/\sqrt{2}$ from the positive peak of the electric field signal, ~587 fs at $1/\sqrt{2}$ from the first negative peak of the electric field signal, and ~287 fs from the second negative part of the signal, which corresponds to a frequency range of 100 GHz to 4 THz as seen in Fig. 1. The output power of the THz system (~1 μW) used in this work and the short time of exposure make it biologically safe and provides negligible heating even in high-absorption samples [17]. In all measurements, the sample chamber is purged with dry nitrogen gas for at least 15 minutes to eliminate absorption by water vapor.

THz spectroscopy is used to calculate the complex refractive index of the carbon-based particles embedded in polymer and of tissue phantoms with and without contrast agents. This complex refractive index is defined by:

$$\tilde{n}=n-i\kappa=n-i\frac{c}{\omega}\frac{\alpha_{abs}}{2} \quad (1)$$

Where is $\tilde{n}$ the complex refractive index, n is the real part of the refractive index (referred to here as just refractive index), κ is the imaginary part of the refractive index or extinction coefficient, c is the speed of light, ω is the angular frequency, and α_{abs} is the absorption coefficient. In this work the standard optical properties of refractive index and absorption coefficient are presented. The sample setup for spectroscopy can be seen in Fig. 2. For particles embedded in polymers, the background media are rigid and free-standing so the

transmitted signal through the sample can be measured directly as seen in Fig. 2a. The Fourier transform of the transmitted signal is then compared to the signal transmitted through the empty sample holder based on the following equation [23]:

$$E_{samp}/E_{ref}=\tilde{\tau}e^{(\gamma_1-\gamma_2)d} \quad (2)$$

Where E_{samp} is the transmitted electric field signal through the sample, E_{ref} is the transmitted reference signal, γ_1 and γ_2 are the complex propagation constants defined by $\gamma=i\frac{\omega}{c}\tilde{n}$ for the background medium (air) and the sample respectively, d is the sample thickness, and $\tilde{\tau}$ is the ratio of the Fresnel transmission terms for the sample and reference setups. A range of refractive index and absorption coefficient values are inserted into equation (2) and compared against the measurement data to find the pair of values with the lowest total mean square error at each frequency. It is important to note that the refractive indices and absorption coefficients calculated in this work are for both the particles and the background medium. The standard practice is to suspend or mix these particles with another medium such as PDMS or polyethylene, though it is possible to extract the optical properties of the particles alone as reported in [51]. More detailed equations for calculating the refractive index and absorption coefficient from transmitted signals were published in [23].

For phantoms, the samples are not rigid and are instead mounted between quartz windows with a spacer to ensure consistent sample thickness, as seen in Fig. 2b. In this setup, the reference measurement is taken from the transmitted signal through two quartz windows without the phantom (Fig, 2b), and the solution of the refractive index and absorption coefficient follow the same form as equation (2). All spectroscopy measurements use an average of 1800 transmitted signals. All phantom samples used in the spectroscopy measurements between the two quartz windows in this work are 200 μm thick.

2.2 Breast Cancer Phantom Tissue Development

The development of phantom materials in THz band was reported in the literature [47,48]. We developed phantom materials with THz properties similar to that of freshly excised tissue using TX151 solidifying powder (obtained from Oil Center Research, Inc.) mixed with agar and an emulsion of water, olive oil, and a surfactant [49,50]. An effective dielectric permittivity equation is used to obtain the first estimate for how much oil should be incorporated to approach the desired THz material properties. Due to oil and water emulsions forming small, spherical micelles when mixed, this estimate is made for spherical packing using Bottcher's equation [52]:

$$\nu_2=\frac{(\tilde{\varepsilon}-\tilde{\varepsilon}_1)(2\tilde{\varepsilon}+\tilde{\varepsilon}_2)}{3\tilde{\varepsilon}(\tilde{\varepsilon}_2-\tilde{\varepsilon}_1)}. \quad (3)$$

Here $\tilde{\varepsilon}$ is the effective complex permittivity of the combined mixture, while $\tilde{\varepsilon}_1$ and $\tilde{\varepsilon}_2$ are the complex permittivity of the host medium (water-surfactant-TX151) and the permeating material (oil), respectively. The permittivity of the individual components and resulting

phantom are obtained using THz spectroscopy. Then these values are used to calculate ν_2, the volume packing fraction. While ν_2 is not inherently known for the mixture, it can be directly related to the volume percentage of oil if the dispersion of oil is assumed to be consistent. The permittivity of a phantom mixture for a given volume percentage can also be estimated by changing the equation to its quadratic form as follows:

$$0=2\tilde{\varepsilon}^2+(3\nu_2(\tilde{\varepsilon}_1-\tilde{\varepsilon}_2)+\tilde{\varepsilon}_2-2\tilde{\varepsilon}_1)\tilde{\varepsilon}-\tilde{\varepsilon}_1\tilde{\varepsilon}_2. \quad (4)$$

The phantoms for this work are detailed in [49,50] and were tuned to the refractive index and absorption coefficient of infiltrating ductal carcinoma (IDC) and healthy fibroglandular tissues reported in the literature [19]. The developed recipe for the IDC phantom by percent weight is 66% water, 12% oil, 6% surfactant, 14% TX151, and 2% agar, and the developed recipe for the fibroglandular phantom is 56% water, 18% oil, 10% surfactant, 14% TX151, 2% agar [49,50].

2.3 Carbon-based Particle Preparation

The microdiamonds, nanodiamonds (NDs), and nanometer-scale OLC used in this work were provided by Adámas Nanotechnologies in two different media. The first set of particles was embedded in PDMS while subsequent samples were received as a powder. All nanometer-scale properties were evenly distributed in the PDMS composites while the microdiamonds were too heavy to remain in suspension and sedimented into a single layer before the PDMS was cured. While a single layer of microdiamonds in PDMS does not fully model the distributed particles that would be present in a biomedical application, it is still useful to observe the THz signal interaction with the particles. Additional details on the fabrication of particles and sample preparation were previously reported in other works [32], [37],[39],[53].

Four types and concentrations (by weight) of PDMS-nanoparticle composites were investigated: 1% 100 nm diameter OLC, 1% 100 nm diameter NDs, 2% 100 nm diameter NDs, and 1% 40 nm diameter NDs. For microdiamonds in a single layer in PDMS, three particle types and treatments were investigated: 10% 100 μm diameter pristine microdiamonds, 5% 150 μm diameter irradiated (Irr) microdiamonds, and 10% 150 μm diameter irradiated and annealed (Irr-Ann) microdiamonds containing NV centers.

2.4 THz Spectroscopy Process

Following an initial investigation of the different particle types in PDMS, the particles that showed potential as THz image contrast agents were investigated individually by embedding the particles in polyethylene tablets. Microscope photos of a few selected powders are shown in Fig. 3. Fig. 3a shows 100 μm microdiamonds at 100X magnification, with the yellow hue being typical of these samples due to the lattice size. The same is seen in the 20 μm microdiamonds at 200X magnification in Fig. 3b, which shows consistent structure and coloration of the particles across different scales and discrete separation of particles. This consistency persists down to the nanodiamond scale as well, though only microdiamonds were received as powder. Fig. 3c shows 200 nm OLC at 400X magnification. Both

individual particles and larger clusters and aggregates can be seen at this scale. This grouping together of particles is often attributed as the reason for the broad frequency response of OLC [37],[39], though it should disperse in aqueous solutions.

The polyethylene tablets with the samples are generated by mixing polyethylene powder and particles in a mortar, then compressing them into tablets using a five-ton hydraulic press. The particles are mixed at a 1% or 10% concentration in polyethylene to examine the degree of interaction the particles have with the THz signal. For the larger microdiamonds, the diameters of some of the particles are comparable with THz wavelengths and result in some scattering as will be shown in Section 3. Therefore, in order to obtain reliable characterization of these particles, all particle-embedded tablets are measured at two different rotations, then broken down and remade multiple times to provide averaged properties with reduced scattering effects. This process is also extended to the nanometer-scale particles to maintain a consistent measurement process for all samples. Spectroscopy of the particles in PDMS and polyethylene is conducted using the single-layer transmission setup with an air reference seen in Fig. 2a.

Following individual characterization, the particles most suitable to providing image contrast are implemented into the developed IDC (cancer) phantom tissues and characterized using the spectroscopy setup in Fig. 2b. Then the particles in the phantoms are used for THz imaging to simulate the contrast agent binding to the surface of excised breast cancer tumors.

3. Results of Particle Characterization

3.1. Particles in PDMS

The first set of particles examined are embedded in PDMS and investigated separately as nanometer-scale particles and micrometer-scale particles. THz spectroscopy of the four PDMS-nanoparticle composite samples and a pure PDMS sample, as a reference, is shown in Fig. 4. The optical properties of bulk diamond from [54] are reported in Figs. 4-9 for comparison.

All the nanometer-scale particles show an increase in the refractive index compared to the PDMS without particles in Fig. 4a. The use of PDMS as a reference serves as a relatively low absorption background to observe the THz interaction with each particle type. It is clearly seen that the increase provided by the NDs is relatively small while the shift provided by OLC is more significant. A similar change in properties is seen in the absorption coefficient in Fig. 4b. Here the NDs provide no noticeable increase in absorption, which agrees with the low absorption of bulk diamond, while the OLC significantly increases the absorption coefficient of the overall sample. Therefore, for particles in the nanometer size range, only the OLC shows a significant promise as a THz contrast agent.

The THz spectroscopy results of the four PDMS-microdiamond composites are displayed in Fig. 5, with the refractive index shown in Fig. 5a and the absorption coefficient in Fig. 5b. All three particle types provide an increased refractive index and absorption coefficient over the entire measurement range. The results of Fig. 5 outline the different variables of the

particles that are examined in this work. Most notably, the 150 μm diameter particles demonstrate an increase at lower frequencies compared to pure PDMS and have an absorption coefficient peak around 1.5 THz. Meanwhile the 100 μm diameter particles show a more notable increase at higher frequencies and an absorption peak around 2.75 THz. In both cases the absorption peak most likely indicates a resonance due to the particle sizes coinciding with THz wavelengths. Between the two 150 μm diameter samples, the difference in the properties is due to different particle concentrations. Both OLC and microdiamonds show significant properties in the THz frequency range, but additional spectroscopy is needed to determine the effect of particle size and microdiamond treatment. Since NDs show insignificant reaction to THz signals, they are not considered for subsequent measurements.

3.2. Microdiamonds in Polyethylene

The second round of particles consists of different sizes of OLC and microdiamonds left in powdered form, which are characterized by polyethylene embedding as described in Section 2. The microdiamonds are investigated in diameters of 1, 20, 40, 100, and 150 μm. They are also examined for a variety of treatments based on availability as follows: 1-40 μm particles in pristine, irradiated, and irradiated-annealed states, 100 μm particles in pristine and irradiated states only, and 150 μm particles in irradiated and irradiated-annealed states.

3.2.1. Effect of microdiamond size—Polyethylene tablets are made for each pristine microdiamond ranging from 1 μm to 100 μm with a 10% concentration and measured using the process described in Section 2. The average properties across three tablets for each particle size are presented in Fig. 6.

The results for microdiamonds are shown in Fig. 6, where they demonstrate a noticeable increase in the refractive index for all sizes. The 100 μm particles primarily provide enhancement at lower THz frequencies, while the 40 μm particles show a significant increase across most of the measured frequency range, only dropping back toward the value of polyethylene as the frequency approaches 3.5 THz. Meanwhile the 20 μm and 1 μm particles demonstrate a comparable and uniform increase in the refractive index. The changes to the absorption coefficient in Fig. 6b provide more clarity to the changes in the THz properties of the samples seen previously. For the 100 μm microdiamonds, an absorption peak can be seen around 2.5 THz. This is similar to the size-dependent resonance peak seen for the same particles in the PDMS in Fig. 5, but it is broader and at a slightly lower frequency due to a more even distribution of the particles in polyethylene. This size-dependent scattering is supported by the steadily increasing absorption of the 40 μm particles, which appear to possibly have a peak outside of the frequency range achievable by the system. However, the 1 and 20 μm particles show only a small, uniform increase in the absorption. This discrepancy is most likely due to these particles being too small to scatter the THz signal, leaving the attenuation of the transmitted signal as the only contribution to the calculated absorption. This agrees with the slightly higher shifts in properties created by the 1 μm particles, as they would be present at a higher density in the sample for the same weight concentration.

From the results in Fig. 6, it is seen that either 40 μm or 100 μm particles could potentially increase the contrast of a region in a THz imaging setup. While the 1 μm and 20 μm particles do show some small increase in the refractive index of the material, they provide insignificant changes to the absorption coefficient even in a low-absorption material. For the larger particles, 40 μm microdiamonds show a more broadband shift in the refractive index and absorption coefficient compared to the polyethylene alone, but the 100 μm particles exhibit more significant changes in properties at lower frequencies where most of the power of the THz pulse is present (as seen in the signal spectrum in Fig. 1d). Thus the selection between these two particles is dependent on what is most suitable for the imaging application.

3.2.2. Effect of microdiamond treatment—Since the characterization of microdiamonds embedded in PDMS did not address the effect of different particle treatments on the THz properties, three samples were prepared with the 40 μm microdiamond in pristine, irradiated, and irradiated-annealed states at 10% concentration and measured following the process in Section 2. The results of this characterization are given in Fig. 7 with the polyethylene and average properties from the 100 μm samples as references.

It can be seen in Fig. 7a that the microdiamond treatments have little change to the refractive index from the pristine microdiamond particles. This is also seen in Fig. 7b, where there is a negligible difference between the absorption of the pristine and treated particles. This process was repeated for the 1 μm and 20 μm particles with similar results not shown here, demonstrating that treatment type of the microdiamond particles has no effect on the THz properties of the particles in this case. It is safe to assume that any effect between the different particles is going to be primarily dependent on the size, as seen in Fig. 6, or the concentration, as seen in Fig. 5.

3.3. OLC in Polyethylene

The OLC in powder form was tested in two sizes based on availability: 100 nm diameter and 200 nm diameter. Both sizes of OLC were implemented into polyethylene tablets in concentrations of 1% and 10% and were characterized with THz transmission spectroscopy as shown in Fig. 2a. The resulting sample THz properties are shown in Fig. 8.

Fig. 8a shows that the 1% 100 nm OLC sample creates a uniform increase in the refractive index of the polyethylene tablet across the entire frequency range. Increasing the OLC to 10% shows a further shift in the refractive index from around 1.48 at 1 THz to roughly 1.57. On the other hand, there is very little increase provided by the 1% 200 nm OLC compared to the polyethylene alone. Increasing the amount to 10% shows a significant shift in the refractive index that follows the same trend as the 100 nm particles, but the increase is not as strong. Similar changes are seen in the absorption coefficient in Fig. 8b, with 100 nm OLC showing a larger uniform increase than 200 nm OLC. These results imply that as the size of the OLC decreases, its effect on the transmitted THz signal will increase. OLC can be generated in even smaller sizes than 100 nm, meaning that greater impact by the particles is

possible as the size decreases. However, for the scope of this work, only 100 nm and 200 nm OLC particles could be tested due to availability of these particles.

The contrast between the OLC samples and pure polyethylene can also be compared to the properties of the polyethylene tablet with 40 μm or 100 μm microdiamonds at 10% concentration in Fig. 6. The OLC provides a greater and more uniform shift in both refractive index and absorption coefficient with a lower concentration than both microdiamond sample sizes. In Fig. 8, for 1% OLC the 100 nm particles show slightly higher absorption than the 200 nm particles. The results at 10% concentration are consistent, with 100 nm higher than 200 nm. Both 10% concentrations show higher absorption than the 1%, which is the anticipated result. The higher absorption in the smaller 100 nm particles could be explained due to the multiple reflections of the signal between the particles. For Fig. 6, the same consistency is seen between the smaller microdiamond sizes of 1 μm and 20 μm (1 μm shows slightly higher absorption than 20 μm). However, the results of the 100 μm and 40 μm particles are inconsistent with the above observation. This could be explained by a resonance phenomenon. For example, the wavelength at 2.5 THz is roughly 83 μm in polyethylene which is close to the size of the 100 μm particles and consistent with the peak seen in the absorption coefficient. A peak for the 40 μm particles would be anticipated at a higher frequency which is not seen in the figure (out of range of the plotted data). Thus, while there is some shift in properties associated with microdiamonds in the tested THz band, OLC shows a much greater potential for the purpose of enhanced THz imaging.

3.4. Microdiamonds and OLC in IDC Phantom

So far, the particles were only characterized in relatively low-loss media to observe the THz interaction of the particles alone. To determine the effectiveness of these particles in a high-absorption environment, such as freshly excised breast tissues, the developed breast phantom IDC tissue (cancer-like tissue) is used as a medium here. In this case, since the 100 μm microdiamonds and 100 nm OLC show the most promise of the two particle types, they are investigated in greater detail. The weight of the IDC phantom recipe is calculated such that the particles could be introduced using a 10% concentration for the microdiamonds and a 1% or 10% concentration for the OLC. Each sample with these particles is measured at slices from 6 different locations in the breast phantom tissue in the spectroscopy setup shown in Fig. 2b to obtain an average set of values for these data. The results are shown in Fig. 9 and are compared to the phantom without particles. It should be noted that the frequency range for the spectroscopy in Fig. 9 was reduced to 2 THz maximum, instead of 3.5 THz used in the previous results, due to the high losses in the breast phantom tissues causing a significant attenuation of the signal beyond 2 THz. This frequency limit agrees with the reported spectroscopy data of freshly excised human breast tumor tissue [19].

Fig. 9a shows that the refractive index of the IDC phantom tissues increases slightly from the 100 μm microdiamonds at frequencies between 1 and 2 THz. However, the increase is minimal and not enough to provide a significant contrast. The 1% OLC shows a more uniform increase, although small, in the refractive index across the entire frequency range. On the other hand, the phantom with 10% OLC is seen to have a significantly higher refractive index than the IDC phantom alone. The absorption coefficient of the phantoms in

Fig. 9b shows similar trends to refractive index in Fig. 9a. The results indicate that the 100 nm OLC shows the greatest potential for use as a contrast agent out of all the particles tested in this work, as it shows a noticeable change in the properties of the IDC phantom even in low concentrations.

It should be noted that there is a difference in refractive index between the 10% 100 nm OLC in the IDC phantom in Fig. 9a and the 10% 100 nm OLC in polyethylene in Fig. 8a, especially at lower frequencies. This is due to the nature of the background material, as the OLC is seen to provide a consistent increase over the pure polyethylene or over the IDC phantom without particles. For OLC, this shift in the refractive index is seen to be more significant at lower frequencies in Fig. 8a. This low frequency emphasis combined with the high refractive index at low frequencies in the IDC phantom generates the very strong increase seen in the phantom with OLC added in Fig. 9a.

4. Results of Breast Phantom Tumor Imaging with and without OLC Particles

Due to the significant THz interaction observed for the 100 nm OLC in PDMS, polyethylene, and in IDC phantom background media, it is selected for use in a THz reflection mode imaging setup to examine the practical contrast improvement potential of these particles. The setup is similar to that of Fig. 1a but with the signal reflected from the sample as seen in Fig. 1b. As an initial test, four breast phantom tissues are developed following our recipe in [49] and [50] and compared in Fig. 10. The four samples are made as follows: one fibroglandular phantom without particles, one IDC phantom without particles, one IDC phantom with 1% 100 nm OLC, and one IDC phantom with 10% 100 nm OLC. Since OLC can be functionalized to selectively bind to cancer cells, only OLC implementation into the cancer phantom is investigated here. A THz raster scan is performed of each phantom at step size of 400 μm, and the results are shown in Fig. 10. All THz images are generated by taking the peak value of the reflected electric field signal at each pixel and normalizing by the peak value of the incident signal [23-25]. Fig. 10a shows the reflection for the fibro phantom. It should be noted that there is some amount of random noise present in the THz image despite being a solid phantom, which is primarily due to sample surface roughness creating small air pockets between the phantom and the polystyrene plate used for holding the sample. This roughness is a common challenge in fresh tissue as well, as an uneven tissue surface can result in air gaps with the polystyrene plate as was observed in our previous work [24]. While several attempts were made to minimize the roughness and associated noise in the phantom, thus far it has not been fully resolved and therefore appears in all phantom imaging in this work. Fig. 10b shows the THz image of the IDC phantom without the particles. It should be noted that the reflected field from the IDC phantom inherently shows slightly higher values than the fibro phantom, as is indicated by the slight change of field color from light blue to yellow. This corresponds to a fibro reflection between 0.14 and 0.17 in arbitrary units of the electric field compared to the 0.17 to 0.2 seen in the IDC phantom, which is expected due to the challenging difference in the THz properties between the two tissue types. In all figures there is a rim of higher

reflection seen in the red color surrounding each phantom that corresponds to a Teflon spacer used to contain the phantoms while they were being held down for imaging.

Fig. 10c shows a THz image of an IDC phantom with the same recipe as Fig. 10b but with 1% 100 nm OLC added. Here the reflected field is shown to increase to values closer to 0.2 units, which provides greater contrast against the fibro phantom than the IDC phantom alone, although the change in values is small. Finally, the THz image of the IDC phantom with 10% OLC is shown in Fig. 10d. In this case a significant increase in the reflection of the phantom is seen, with an improvement in reflected field of nearly 50% from the IDC phantom alone shown in Fig. 10b. The small area of higher reflection on the left side of the sample in Fig. 10d is most likely due to accumulated OLC that did not uniformly distribute in the phantom. The potential of OLC as an effective contrast agent in THz imaging is consistent with the increases observed in the refractive index and absorption coefficient seen in Fig. 9.

To investigate the effectiveness of the OLC as a contrast agent when dispersed through adjacent IDC and fibroglandular (fibro) tissues, a three-dimensional phantom tumor model is developed as shown in Fig. 11. IDC phantoms with and without OLC are generated (Fig. 11a) and wrapped in a fibroglandular phantom to simulate a highly fibrous margin as shown in Fig. 11b. For developing the phantom tumors with OLC, particles are added and mixed with the IDC phantom in either 1% or 10% concentrations. The phantom tumor bulk is then bisected to expose a surface with adjacent IDC and fibro phantom tissues for imaging as seen in Fig. 11c. Finally, the phantom is scanned in the reflection mode as shown in Fig. 11d. While the THz signal has experimentally shown penetration up to 300 μm in the fibro phantom for reflection imaging of hidden IDC phantoms, this application is focused on imaging just the surgical edge of excised tissue and not for scanning human bodies. Therefore, this setup is selected to emulate THz imaging of freshly excised tissues similar to our ongoing research using fresh animal and human excised tumors.

Figs. 12a-c show the photographs of the phantom tumors including the IDC phantom without OLC, the IDC phantom with 1% OLC, and the IDC phantom with 10% OLC, respectively. For these photos, the fibro phantom is dyed with green food coloring while the IDC phantom is dyed with red food coloring for comparison. These colors have no effect on THz signals. However, for the IDC phantoms containing OLC, the color of the carbon particles make the phantom appear grey or black instead. The THz images are given for the sample without OLC in Fig. 12d, with 1% OLC in Fig. 12e, and with 10% OLC in Fig. 12f. All images are produced using the same normalized reflection peak against the incident peak as described for Fig. 10. For each THz image, the outline of the IDC region in the photograph was superimposed as a dashed line to compare the regions of the phantom. The comparison between the IDC and fibro phantoms without OLC in Figs. 12a and 12d shows that there is some distinction between the two regions. However, the contrast is low, and the noise attributed to the surface roughness of the phantom causes dips in the IDC below the values of the fibro which serves as an additional challenge in interpreting the THz image. The sample with 1% OLC in Figs. 12b and 12e shows faint contrast between the two regions as well. This is expected from the 1% OLC showing a relatively small effect in the spectroscopy of the phantom in Fig. 9 and in the image in Fig. 10c. Finally, the sample with

10% OLC in Figs. 12c and 12f shows a drastically increased reflection for the IDC phantom compared to the surrounding fibro phantom and compared to the sample without OLC. This increase in reflection in Fig. 12f is consistent with spectroscopy of the phantom with 10% OLC in Fig. 9 due to the strong increase in the refractive index and absorption coefficient, which both increase the reflected signal. Here the reflection of the IDC phantom is almost doubled compared with that of the other two samples, while the fibro phantom is approximately the same. Therefore, the OLC in a 10% concentration is shown to be a potential contrast agent in THz imaging of breast cancer.

5. Conclusions

This work has investigated various carbon-based particles as potential contrast agents in THz imaging. Overall, OLC demonstrates the greatest interaction with the THz signal compared with microdiamonds and nanodiamonds investigated in the same background medium. Also THz imaging of 10% OLC in cancer phantoms shows greater enhancement of the THz response than other nanoparticles used in THz imaging without the need for external sources as reported in the literature [27-29]. Other works showed that OLC is suitable for functionalization that would cause them to selectively bind to cancer cells, making it promising for future investigations in THz margin assessment of breast cancer and possible other types of cancer [40]. The significance of the OLC 100 nm results presented here is that their size is a fraction of the THz wavelengths used in this work. The broadband interaction of OLC with electromagnetic waves, despite its sub-wavelength size, was attributed to its physical features at multiple sizes including defects in the onion-like layers, the overall aggregate size of the particles, and the interaction of larger conglomerates of adjacent OLC particles due to the graphene-like structure of the outer layers [37],[39].

The use of OLC as a THz contrast agent primarily depends on the size and safety limitations of the particles [41],[42]. Thus far there is relatively little research into the biological safety of OLC. For higher concentrations reported in literature, 6 mg/L (0.6% by weight in water) of 30 nm OLC showed some concerns of gene damage but less than carbon nanotubes [42], and 3000 μg/mL (0.3% by weight in water) showed only a minor reduction in cell viability [43]. Compared to the highest reported concentration of 0.6% 30 nm OLC, the same number of 100 nm OLC particles would be ~22% by weight in water. Thus, the concentrations reported in this work are feasible; however, additional research is needed. Trends in the spectroscopy of OLC imply that smaller sizes may provide even greater contrast than the 100 nm particles investigated here. As such, future work will focus on particle injection in animal model (murine) in vivo to investigate toxicity and safe particle concentration, and additional work is being conducted to measure the sensitivity and specificity of THz imaging in fresh tissue applications.

Acknowledgments

This work was funded in part by NSF/ECCS award #140800, NSF/DGE award #1450079, NIH award R15CA208798, and the University of Arkansas Distinguished Doctoral Fellowship. The pulsed THz system used in this work was funded by NSF/MRI award #1228958.

References

1. Hassan AM, El-Shenawee M. Review of Electromagnetic Techniques for Breast Cancer Detection. IEEE Rev Biomed Eng. 2011; 4:103–118. DOI: 10.1109/RBME.2011.2169780 [PubMed: 22273794]
2. Surowiec AJ, Stuchly SS, Barr JR, Swarup A. Dielectric Properties of Breast Caricinoma and the Surrounding Tissues. IEEE Trans Biomed Eng. 1988; 35(4):257–263. DOI: 10.1109/10.1374 [PubMed: 2834285]
3. Joines WT, Zhang Y, Li C, Jirtle RL. The measured electrical properties of normal and malignant human tissues from 50 to 900 MHz. Med Phys. 1994; 21(4):547–550. DOI: 10.1118/1.597312 [PubMed: 8058021]
4. Choi JW, Cho J, Lee Y, Yim J, Kang B, Oh KK, Jung WH, Kim HJ, Cheon C, Lee H, Kwon Y. Microwave detection of metastasized breast cancer cells in the lymph node; potential application for sentinel lymphadenectomy. Breast Cancer Res Treat. 2004; 86(2):107–115. DOI: 10.1023/B:BREA.0000032979.52773.fb [PubMed: 15319563]
5. Campbell AM, Land DV. Dielectric properties of female human breast tissue measured in vitro at 3.2 GHz. Phys Med Biol. 1992; 37(1):193–210. DOI: 10.1088/0031-9155/37/1/014 [PubMed: 1741424]
6. Lazebnik M, McCartney L, Popovic D, Watkins CB, Lindstrom MJ, Harter J, Sewall S, Magliocco A, Booske JH, Okoniewski M, Hagness SC. A large-scale study of the ultrawideband microwave dielectric properties of normal breast tissue obtained from reduction surgeries. Phys Med Biol. 2007; 52(10):2637–2656. DOI: 10.1088/0031-9155/52/10/001 [PubMed: 17473342]
7. Lazebnik M, Popovic D, McCartney L, Watkins CB, Lindstrom MJ, Harter J, Sewall S, Ogilvie T, Magliocco A, Breslin TM, Temple W, Daphne M, Booske JH, Okoniewski M, Hagness SC. A large-scale study of the ultrawideband microwave dielectric properties of normal, benign and malignant breast tissues obtained from cancer surgeries. Phys Med Biol. 2007; 52(20):6093–6115. DOI: 10.1088/0031-9155/52/20/002 [PubMed: 17921574]
8. Peters VG, Wymant DR, Patterson MS, Frank GL. Optical properties of normal and diseased human breast tissues in the visible and near infrared. Phys Med Biol. 1990; 35(9):1317–1334. DOI: 10.1088/0031-9155/35/9/010 [PubMed: 2236211]
9. Palmer GM, Ramanujam N. Monte Carlo-based inverse model for calculating tissue optical properties. Part II: Application to breast cancer diagnosis. Appl Opt. 2006; 45(5):1072–1078. DOI: 10.1364/AO.45.001072 [PubMed: 16512551]
10. Tummers QRJG, Verbeek FPR, Schaafsma BE, Boonstra MC, van der Vorst JR, Liefers GJ, van de Velde CJH, Frangioni JV, Vahrmeijer AL. Real-time intraoperative detection of breast cancer using near-infrared fluorescence imaging and Methylene Blue. Eur J Surg Oncol. 2014; 40(7):850–858. DOI: 10.1016/j.ejso.2014.02.225 [PubMed: 24862545]
11. Kumar S, Desmedt C, Larsimont D, Sotiriou C, Goormaghtigh E. Change in the microenvironment of breast cancer studied by FTIR imaging. Analyst. 2013; 138(14):4058–4065. DOI: 10.1039/c3an00241a [PubMed: 23662300]
12. Sharma V, Shivalingaiah S, Peng Y, Euhus D, Gryczynski Z, Liu H. Auto-fluorescence lifetime and light reflectance spectroscopy for breast cancer diagnosis: potential tools for intraoperative margin detection. Biomed Opt Express. 2012; 3(8):1825–1840. DOI: 10.1364/BOE.3.001825 [PubMed: 22876347]
13. Layfield DM, May DJ, Cutress RI, Richardson C, Agrawal A, Wise M, Yiangou C. The effect of introducing an in-theatre intra-operative specimen radiography (IOSR) system on the management of palpable breast cancer within a single unit. The Breast. 2012; 21(4):459–463. DOI: 10.1016/j.breast.2011.10.010 [PubMed: 22119488]
14. Bathla L, Harris A, Davey M, Sharma P, Silva E. High resolution intra-operative two-dimensional specimen mammography and its impact on second operation for re-excision of positive margins at final pathology after breast conservation surgery. Amer J Surg. 2011; 202(4):387–394. DOI: 10.1016/j.amjsurg.2010.09.031 [PubMed: 21943945]
15. Britton PD, Sonoda LI, Yamamoto AK, Koo B, Soh E, Goud A. Breast surgical specimen radiographs: How reliable are they? European Journal of Radiology. 2011; 79(2):245–249. DOI: 10.1016/j.ejrad.2010.02.012 [PubMed: 20303687]

16. Rua C, Lebas P, Michenet P, Ouldamer L. Evaluation of lumpectomy surgical specimen radiographs in subclinical, in situ and invasive breast cancer, and factors predicting positive margins. Diagn Interv Imaging. 2012; 93(11):871–877. DOI: 10.1016/j.diii.2012.07.010 [PubMed: 23021868]
17. Wilmink GJ, Grundt JE. Invited Review Article: Current State of Research on Biological Effects of Terahertz Radiation. J Infrared Millim Terahertz Waves. 2011; 32(10):1074–1122. DOI: 10.1007/s10762-011-9794-5
18. Han PY, Cho GC, Zhang XC. Time-domain transillumination of biological tissues with terahertz pulses. Opt Lett. 2000; 25(4):242–244. DOI: 10.1364/OL.25.000242 [PubMed: 18059842]
19. Ashworth PC, Pickwell-MacPherson E, Provenzano E, Pinder SE, Purushotham AD, Pepper M, Wallace VP. Terahertz pulsed spectroscopy of freshly excised human breast cancer. Opt Express. 2009; 17(15):12444–12454. DOI: 10.1364/OE.17.012444 [PubMed: 19654646]
20. Fitzgerald AJ, Wallace VP, Jimenez-linan M, Bobrow L, Pye RJ, Purushotham AD. Terahertz Pulsed Imaging of human breast tumors. Radiology. 2006; 239(2):533–540. DOI: 10.1148/radiol.2392041315 [PubMed: 16543586]
21. Woodward RM, Wallace VP, Pye RJ, Cole BE, Arnone DD, Lin EH, Pepper M. Terahertz Pulse Imaging of ex vivo Basal Cell Carcinoma. J Invest Dermatol. 2003; 120(1):72–78. DOI: 10.1046/j.1523-1747.2003.12013.x [PubMed: 12535200]
22. Yamaguchi S, Fukushi Y, Kubota O, Itsuji T, Ouchi T, Yamamoto S. Brain tumor imaging of rat fresh tissue using terahertz spectroscopy. Sci Rep. 2016; 6:1–6. DOI: 10.1038/srep30124 [PubMed: 28442746]
23. Bowman T, El-Shenawee M, Campbell LK. Terahertz transmission vs reflection imaging and model-based characterization for excised breast carcinomas. Biomed Opt Express. 2016; 7(9):3756–3783. DOI: 10.1364/BOE.7.003756 [PubMed: 27699136]
24. Bowman TC, El-Shenawee M, Campbell LK. Terahertz Imaging of Excised Breast Tumor Tissue on Paraffin Sections. IEEE Trans Antennas Propag. 2015; 63(5):2088–2097. DOI: 10.1109/TAP.2015.2406893
25. Bowman T, Wu Y, Gauch J, Campbell LK, El-Shenawee M. Terahertz Imaging of Three-Dimensional Dehydrated Breast Cancer Tumors. Journal of Infrared, Millimeter, and Terahertz Waves. 2017; 38(6):766–786. DOI: 10.1007/s10762-017-0377-y
26. Miura Y, Kamataki A, Uzuki M, Sasaki T, Nishizawa J, Sawai T. Terahertz-wave spectroscopy for precise histopathological imaging of tumor and non-tumor lesions in paraffin sections. Tohoku J Exp Med. 2011; 223(4):291–296. DOI: 10.1620/tjem.223.291 [PubMed: 21467828]
27. Oh SJ, Kang J, Maeng I, Suh JS, Huh YM, Haam S, Son JH. Nanoparticle-enabled terahertz imaging for cancer diagnosis. Opt Express. 2009; 17(5):3469–3475. DOI: 10.1364/OE.17.003469 [PubMed: 19259185]
28. Park JY, Choi HJ, Nam G, Cho K, Son J. In Vivo Dual-Modality Terahertz/Magnetic Resonance Imaging Using Superparamagnetic Iron Oxide Nanoparticles as a Dual Contrast Agent. IEEE Trans Terahertz Sci Technol. 2012; 2(1):93–98. DOI: 10.1109/TTHZ.2011.2177174
29. Zhang R, Zhang L, Wu T, Zuo S, Wang R, Zhang J, Fang J. Contrast-enhanced continuous-terahertz-wave imaging based on superparamagnetic iron oxide nanoparticles for biomedical applications. Opt Express. 2016; 24(8):7915–7921. DOI: 10.1364/OE.24.007915 [PubMed: 27137233]
30. Lee DK, Kim H, Kim T, Cho B, Lee K, Son JH. Characteristics of gadolinium oxide nanoparticles as contrast agents for terahertz imaging. J Infrared Millim Terahertz Waves. 2011; 32(4):506–512. DOI: 10.1007/s10762-011-9776-7
31. Ney M, Abdulhalim I. Ultrahigh polarimetric image contrast enhancement for skin cancer diagnosis using InN plasmonic nanoparticles in the terahertz range. J Biomed Opt. 2015; 20(12):125007.doi: 10.1117/1.JBO.20.12.125007 [PubMed: 26720872]
32. Hui YY, Chang HC. Recent Developments and Applications of Nanodiamonds as Versatile Bioimaging Agents. J Chinese Chem Soc. 2014; 61(1):67–76. DOI: 10.1002/jccs.201300346
33. Giordani S, Bartelmess J, Frasconi M, Biondi I, Cheung S, Grossi M, Wu D, Echegoyen L, O'Shea DF. NIR fluorescence labelled carbon nano-onions: synthesis, analysis and cellular imaging. J Mater Chem B. 2014; 2:7459–7463. DOI: 10.1039/C4TB01087F

34. Vaijayanthimala V, Cheng PY, Yeh SH, Liu KK, Hsiao CH, Chao JI, Chang HC. The long-term stability and biocompatibility of fluorescent nanodiamond as an in vivo contrast agent. Biomaterials. 2012; 33(31):7794–7802. DOI: 10.1016/j.biomaterials.2012.06.084 [PubMed: 22863379]
35. Xing Y, Xiong W, Zhu L, Osawa E, Hussin S, Dai L. DNA Damage in Embryonic Stem Cells Caused by Nanodiamonds. ACS Nano. 2011; 5(3):2376–2384. DOI: 10.1021/nn200279k [PubMed: 21370893]
36. Bartelmess J, Quinn SJ, Giordani S. Carbon nanomaterials: multi-functional agents for biomedical fluorescence and Raman imaging. Chem Soc Rev. 2014; 44:4672–4698. DOI: 10.1039/C4CS00306C
37. Macutkevic J, Banys J, Moseenkov S, Kuznetsov V, Nunn N, Shenderova O. Dielectric Properties of Onion-Like Carbon and Detonation Nanodiamond/Polydimethysiloxane Composites. Polym Compos. 2014; 36(11):1–9. DOI: 10.1002/pc.23119
38. Kranauskaite I, Macutkevic J, Banys J, Talik E, Kuznetsov V, Nunn N, Shenderova O. Synergy effects in the electrical conductivity behavior of onion-like carbon and multiwalled carbon nanotubes composites. Phys Status Solidi B. 2015; 252(8):1–5. DOI: 10.1002/pssb.201451745
39. Shenderova O, Grishko V, Cunningham G, Moseenkov S, McGuire G, Kuznetsov V. Onionlike carbon for terahertz electromagnetic shielding. Diam Relat Mater. 2008; 17(4-5):462–466. DOI: 10.1016/j.diamond.2007.08.023
40. Frasconi M, Marotta R, Markey L, Flavin K, Spampinato V, Ceccone G, Echegoyen L, Scanlan EM, Giordani S. Multi-Functionalized Carbon Nano-onions as Imaging Probes for Cancer Cells. Chem Eur J. 2015; 21(52):19071–19080. DOI: 10.1002/chem.201503166 [PubMed: 26577582]
41. Yang M, Flavin K, Kopf I, Radics G, Hearnden CHA, McManus GJ, Moran B, Villalta-Cerdas A, Echegoyen LA, Giordani S, Lavelle EC. Functionalization of Carbon Nanoparticles Modulates Inflammatory Cell Recruitment and NLRP3 Inflammasome Activation. Small. 2013; 9(24):4194–4206. DOI: 10.1002/smll.201300481 [PubMed: 23839951]
42. Ding L, Stilwell J, Zhang T, Elboudwarej O, Jiang H, Selegue JP, Cooke PA, Gray JW, Chen FF. Molecular Characterization of the Cytotoxic Mechanism of Multiwall Carbon Nanotubes and Nano-Onions on Human Skin Fibroblast. Nano Lett. 2005; 5(12):2448–2464. DOI: 10.1021/nl051748o [PubMed: 16351195]
43. Luszczyn J, Plonska-Brzezinska ME, Palkar A, Dubis AT, Simionescu A, Simionescu DT, Kalska-Szostko B, Winkler K, Echegoyen L. Small noncytotoxic carbon nano-onions: First covalent functionalization with biomolecules. Chem - A Eur J. 2010; 16(16):4870–4880. DOI: 10.1002/chem.200903277
44. Bartelmess J, Giordani S. Carbon nano-onions (multi-layer fullerenes): Chemistry and applications. Beilstein J Nanotechnol. 2014; 5(1):1980–1998. DOI: 10.3762/bjnano.5.207 [PubMed: 25383308]
45. Ito K, Furuya K, Okano Y, Hamada L. Development and Characteristics of a Biological Tissue-Equivalent Phantom for Microwaves. Electron Commun Japan Part I Commun. 2001; 84(4):67–77. DOI: 10.1002/1520-642420010484:4<67::AID-ECJA8>3.0.CO;2-D
46. Lazebnik M, Madsen EL, Frank GR, Hagness SC. Tissue-mimicking phantom materials for narrowband and ultrawideband microwave applications. Phys Med Biol. 2005; 50(18):4245–4258. DOI: 10.1088/0031-9155/50/18/001 [PubMed: 16148391]
47. Walker GC, Berry E, Smye SW, Brettle DS. Materials for phantoms for terahertz pulsed imaging. Phys Med Biol. 2004; 49(21):N363–N369. DOI: 10.1088/0031-9155/49/21/N01 [PubMed: 15584535]
48. Reid, C., Gibson, AP., Hebden, JC., Wallace, VP. An oil and water emulsion phantom for biomedical terahertz spectroscopy. Proc 4th IEEE-EMBS Intl Summer School and Symposium on Medical Devices and Biosensors; 2007. p. 25-28.
49. Walter A, Bowman T, El-Shenawee M. Development of breast cancer tissue phantoms for terahertz imaging. Proc SPIE. 2016; 9700:970003.doi: 10.1117/12.2211176
50. Walter, A. Development of Breast Tissue Phantoms for Enhanced Terahertz Imaging Utilizing Microdiamond and Nano-Onion Particles. University of Arkansas; 2017.

51. Tomita S, Fujii M, Hayashi S. Optical extinction properties of carbon onions prepared from diamond nanoparticles. Phys Rev B. 2002; 66(25):245424.doi: 10.1103/PhysRevB.66.245424

52. Lal K, Parshad R. The permittivity of heterogeneous mixtures. J Phys D Appl Phys. 1973; 6(11): 1363–1368. DOI: 10.1088/0022-3727/6/11/311

53. Macutkevic J, Kranauskaite I, Banys J, Moseenkov S, Kuznetsov V, Shenderova O. Metal-insulator transition and size dependent electrical percolation in onion-like carbon/polydimethylsiloxane composites. J Appl Phys. 2014; 115(21):213702.doi: 10.1063/1.4880995

54. Kubarev VV. Optical properties of CVD-diamond in terahertz and infrared ranges. Nucl Instr Meth Phys Res A. 2009; 603(1-2):22–24. DOI: 10.1016/j.nima.2008.12.121

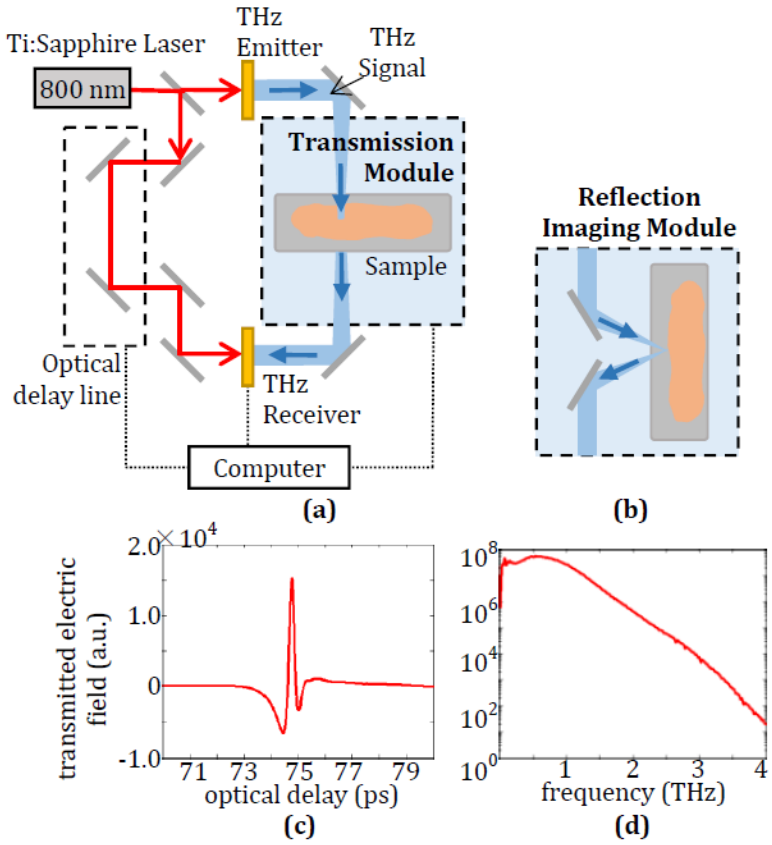

Fig. 1.

(a) Terahertz system diagram with transmission spectroscopy module and (b) reflection imaging module. (c) Generated time-domain THz signal and (d) frequency-domain spectrum after Fourier transform.

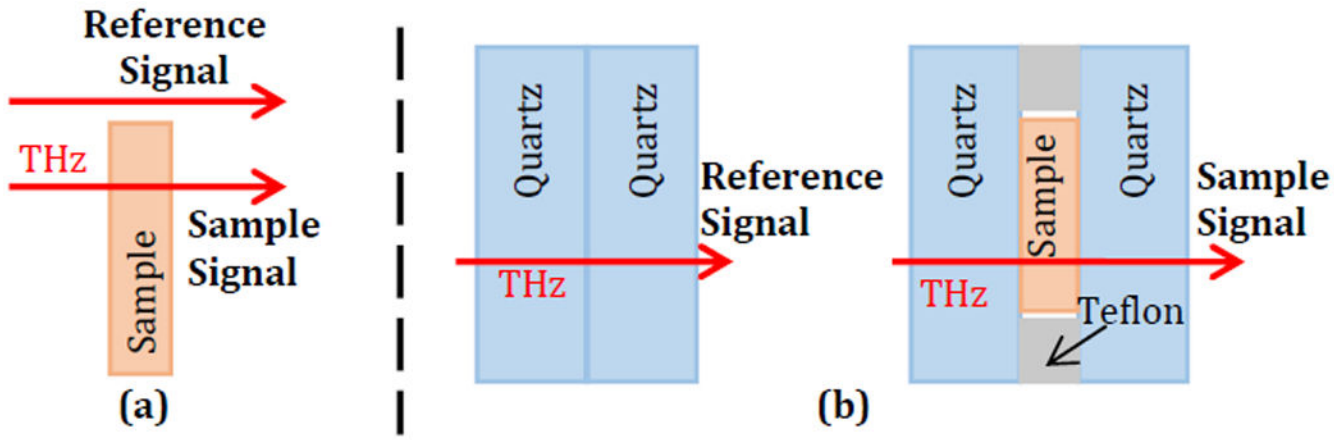

Fig. 2.

THz transmission spectroscopy setups with (a) air reference and single-layer sample transmission for polymer-embedded samples and (b) quartz window reference and multi-layer sample transmission for phantom samples.

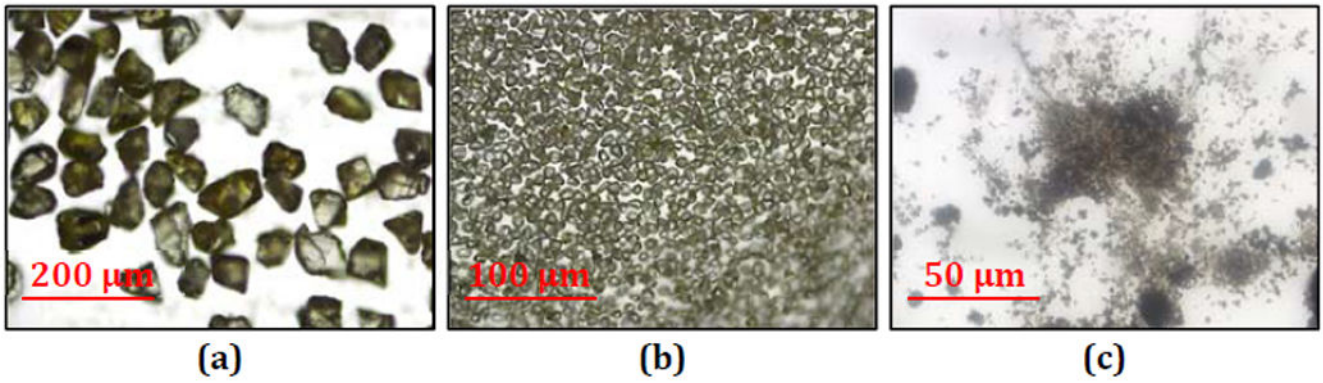

Fig. 3.

Microscope images of powders used in work. (a) 100 µm microdiamond at 100X magnification, (b) 20 µm microdiamond at 200X magnification, and (c) 200 nm OLC at 400X magnification.

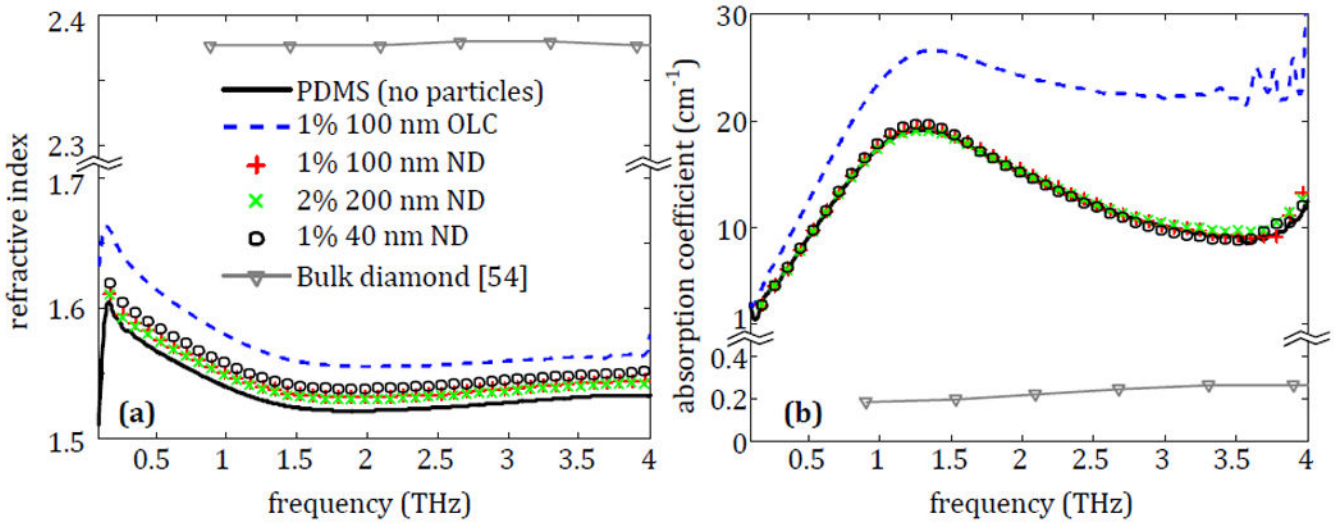

Fig. 4.

The (a) refractive index and (b) absorption coefficient of nanodiamond (ND) and onion-like carbon (OLC) particles embedded in PDMS.

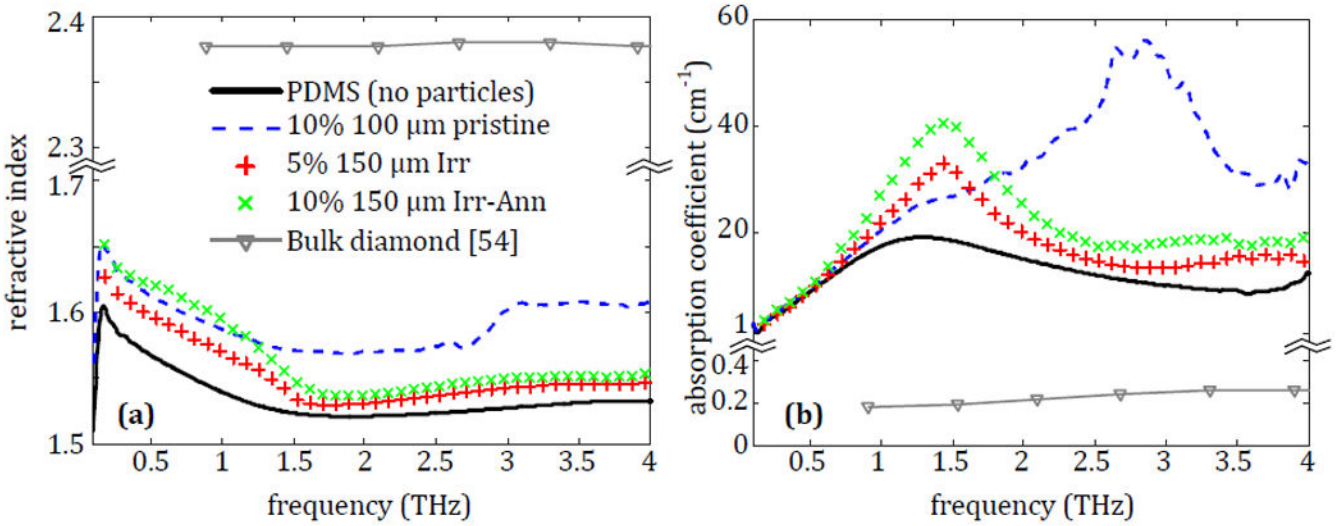

Fig. 5.

The (a) refractive index and (b) absorption coefficient of microdiamonds embedded in PDMS.

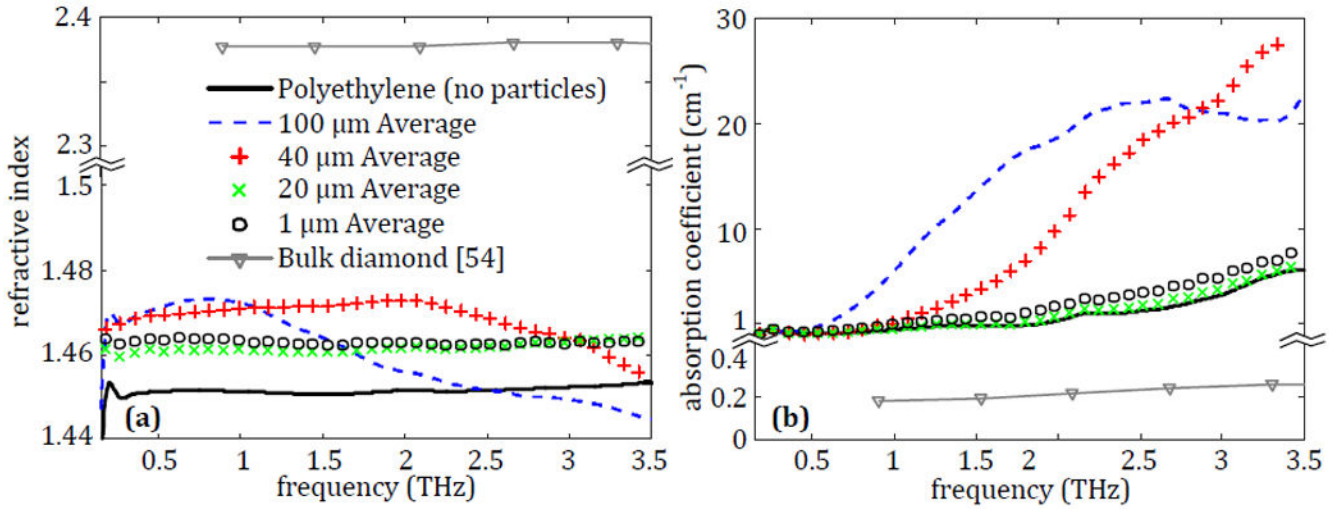

Fig. 6.

The average (a) refractive index and (b) absorption coefficient for polyethylene tablets containing 10% pristine 100 μm diamond, 40 μm diamond, 20 μm diamond or 1 μm diamond.

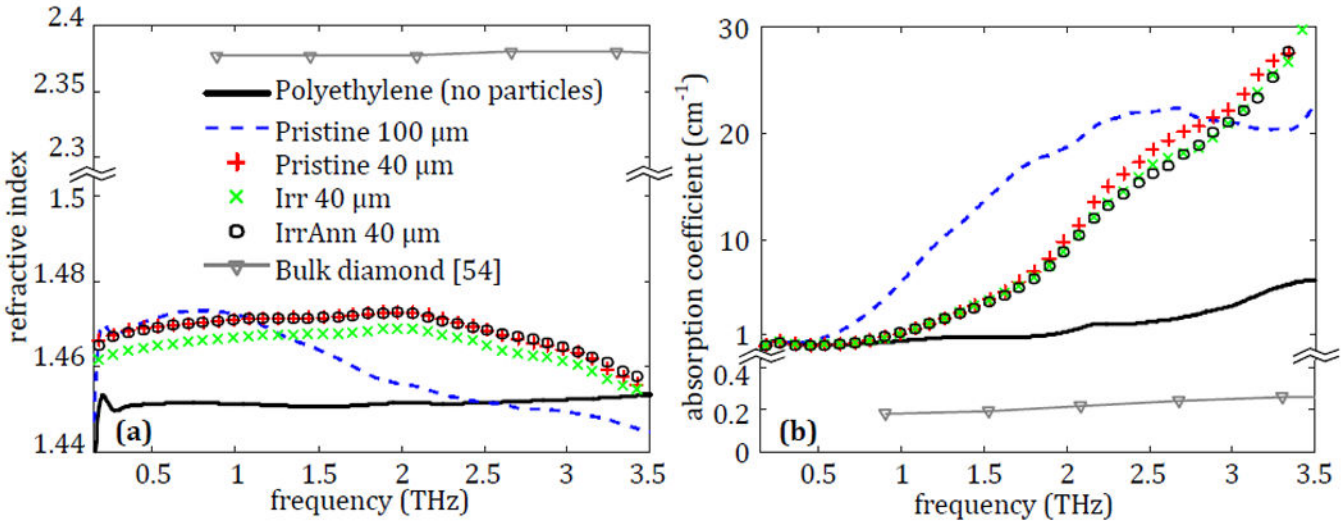

Fig. 7.

The average (a) refractive index and (b) absorption coefficient for polyethylene tablets containing 10% pristine 100 µm diamond, pristine 40 µm diamond, Irr 40 µm diamond or Irr-Ann 40 µm diamond.

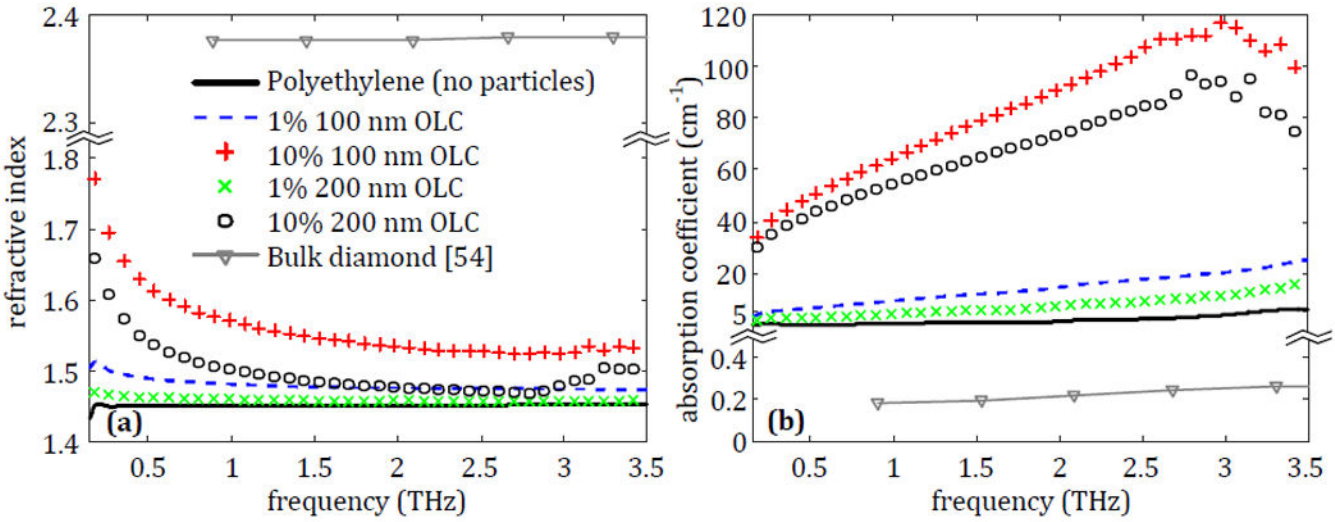

Fig. 8.

The average (a) refractive index and (b) absorption coefficient for polyethylene tablets containing 1% or 10% of either 100 nm or 200 nm OLC.

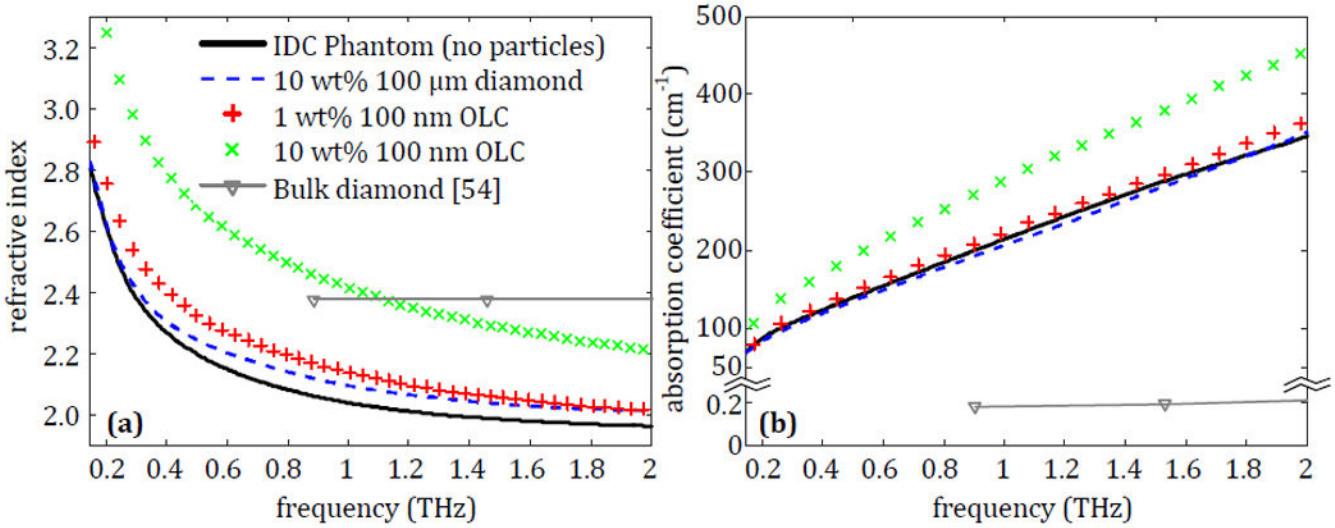

Fig. 9.

The average refractive index and absorption coefficient for IDC phantoms that contain either 10% of pristine 100 µm diamond, 1% of 100 nm OLC or 10% of 100 nm OLC.

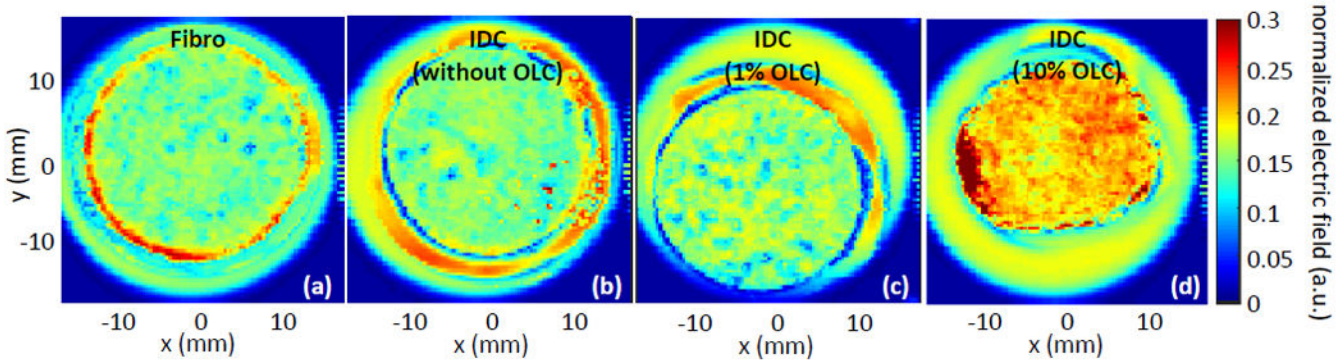

Fig. 10.

THz reflection images of single phantoms generated by taking the reflection peak normalized to the incident signal peak. (a) Fibro phantom with no OLC, (b) IDC phantom with no OLC, (c) IDC phantom with 1% 100 nm OLC, and (d) IDC phantom with 10% 100 nm OLC.

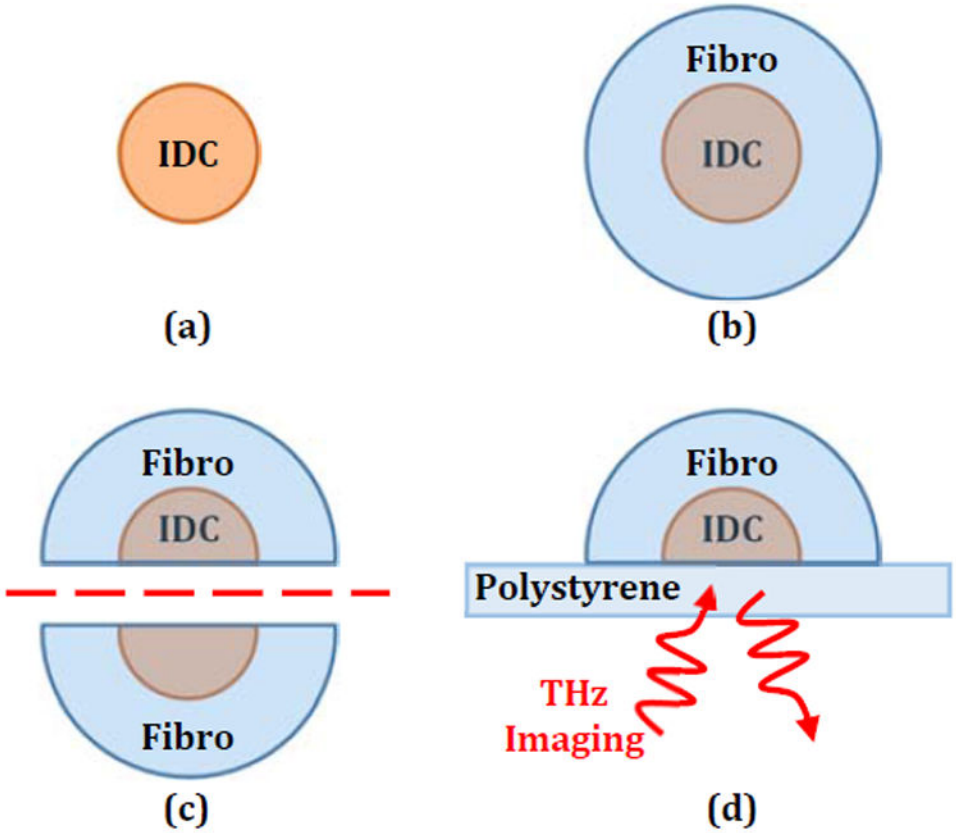

Fig. 11.

Steps in phantom tumor model formation with (a) IDC phantom core, (b) phantom fibro surrounding IDC, (c) tumor model bisection, and (d) THz reflection imaging setup where the emitter and detector are below the sample.

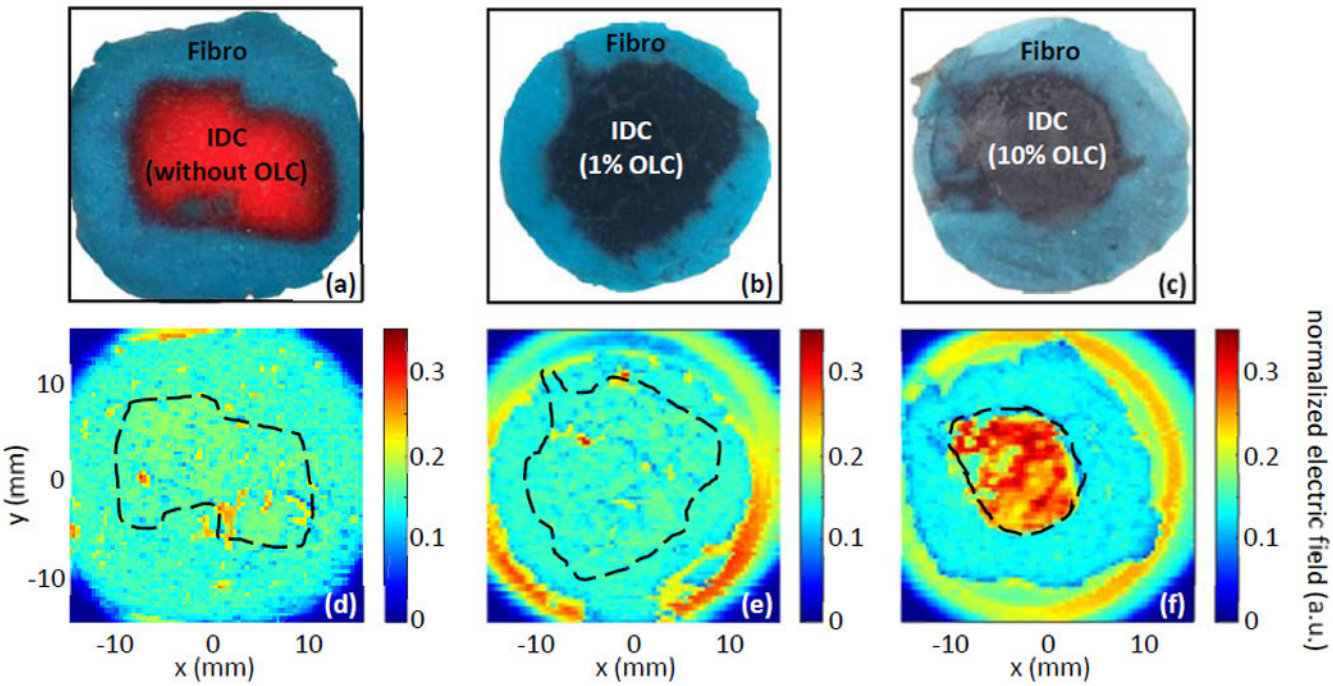

Fig. 12.

THz reflection imaging of combined phantoms shown in photographs for (a) photo of IDC phantom with no OLC, (b) photo of IDC phantom with 1% of 100 nm OLC, and (c) photo of IDC phantom with 10% of 100 nm OLC. THz images in (d-f) show the resulting THz reflection images for (d) no OLC in IDC, (e) 1% OLC in IDC, and (f) 10% OLC in IDC.